Journal of Nanobiotechnology

RESEARCH Open Access

In situ construction of heterojunctions to regulate the biodegradation behavior of copper carriers for tumor-specific cuproptosis-enhanced sono-immunotherapy

Xiqian Cao[1,5†], Lingwei Mao[2†], Yijun Tian[1†], Lang Yan[1,3], Bijiang Geng[4*], Yingtang Zhou[5*] and Jiangbo Zhu[1,3*]

Abstract

Cuproptosis, a novel approach utilizing copper carriers to trigger programmed cell death, exhibits promise for enhancing traditional therapies and activating robust adaptive immune responses. However, the uncontrolled release of Cu ions risks triggering cuproptosis in healthy tissues, potentially causing irreversible damage. To address this, we report on the use of a Cu-MOF (copper metal-organic framework) protective layer to regulate the biodegradation of copper-based nanomaterials. In situ formation of Cu-MOF on Cu_2O nanocubes not only stabilizes the material under physiological conditions but also enhances its sonodynamic therapy (SDT) capabilities by establishing a Z-Scheme heterojunction. Upon SDT activation, the targeted Cu ion release at the tumor site triggers a cascade of reactions, generating reactive oxygen species (ROS) via Fenton-like processes and depleting glutathione (GSH). This ROS surge, combined with effective cuproptosis, modulates the immunosuppressive tumor microenvironment, inducing immunogenic cell death to eliminate primary tumors and inhibit metastasis. This study offers a new paradigm for the controlled integration of SDT, chemodynamic therapy (CDT), cuproptosis, and immunotherapy, achieving precise tumor-targeted treatment via controlled copper nanomaterial degradation.

†Xiqian Cao, Lingwei Mao, and Yijun Tian contributed equally to this work.

*Correspondence:
Bijiang Geng
bjgeng1992@shu.edu.cn
Yingtang Zhou
zhouyingtang@zjou.edu.cn
Jiangbo Zhu
jiangbozhu1@smmu.edu.cn

Full list of author information is available at the end of the article

Graphical abstract

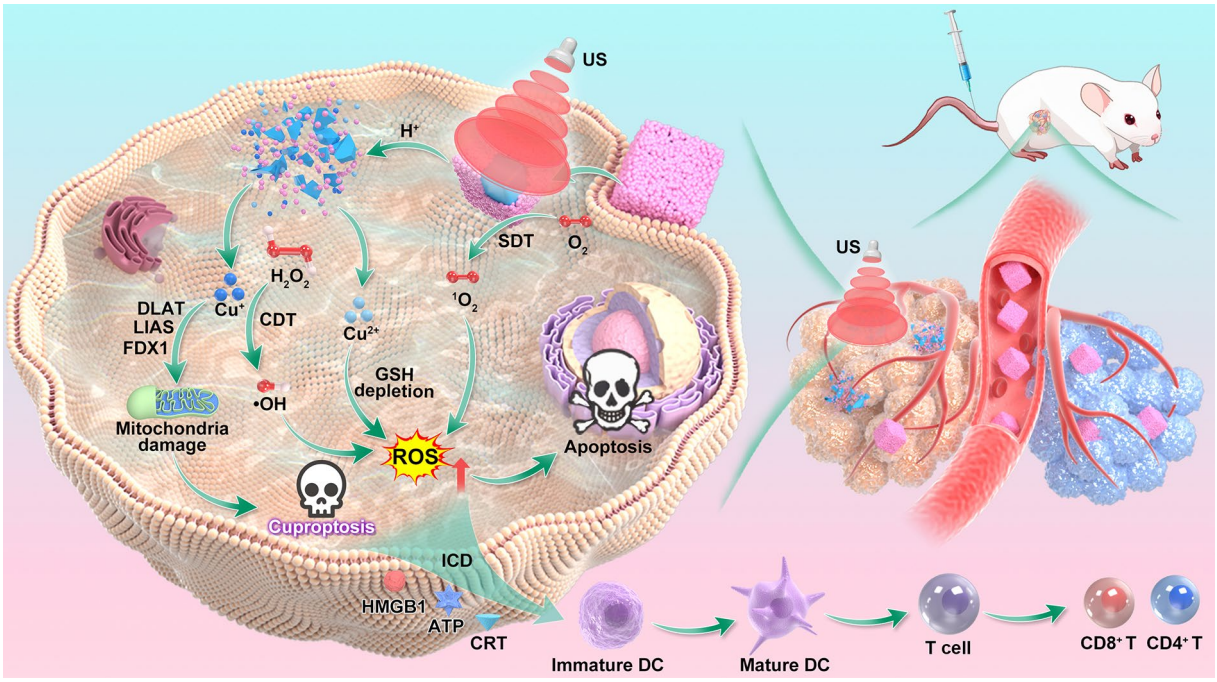

Keywords Cuproptosis, Cu_2O, Sonodynamic therapy, Chemodynamic therapy, Immunotherapy

Introduction

Recurrence and metastasis remain the leading causes of death among cancer patients, making cancer treatment a persistent medical challenge despite ongoing efforts to improve outcomes [1–3]. In contrast to radiotherapy and chemotherapy, which target and destroy cancer cells, immunotherapy works by stimulating the body's immune system to eradicate tumors [4–9]. However, the tumor microenvironment (TME) has become the greatest obstacle to immunotherapy [10–15]. Cold tumors, unlike hot tumors, exhibit an immunosuppressive microenvironment. This environment is characterized by a deficiency of tumor antigens and minimal T-cell infiltration, which aids in immune evasion [16, 17]. To alleviate the constraints imposed by tumor complexity, heterogeneity, and the immunosuppressive TME on immunotherapy, it is crucial to create new types of tumor vaccines and the methods used to manufacture them need to be improved urgently.

The construction of in situ tumor vaccines through the induction of immunogenic cell death (ICD) has become a topic of great interest in recent times [18–20]. The hallmarks of ICD include the redistribution of cell surface molecules, the release of DAMPs, and the activation of immune cells [21–23]. Therefore, research and development of ICD-mediated tumor vaccines are of great significance for advancing immunotherapy [24, 25]. However, traditional treatment modalities primarily induce tumor cell apoptosis, and tumor cells have developed relatively sophisticated anti-apoptotic mechanisms through evolution [26, 27]. The level of tumor antigen release induced by apoptosis is limited, making it difficult to establish a lasting and effective tumor vaccine [28]. Recently, new modes of programmed cell death have been discovered, including ferroptosis, cuproptosis, and necroptosis [29–31]. Unlike apoptosis, ferroptosis, cuproptosis, and necroptosis are intrinsically inflammatory and immunogenic forms of cell death. Thus, exploring the induction methods and effective strategies for new death modes like cuproptosis offers new avenues for constructing ICD-induced tumor vaccines.

Cuproptosis is a unique mechanism of cell death that is copper-dependent, as an abundance of copper ions can prompt cell death by binding to lipoylated proteins [18–34]. Analysis of the mechanisms behind cuproptosis reveals that enhancing the copper ion level in tumor cells is a key factor affecting the efficacy of tumor therapy [35, 36]. To enhance therapeutic effectiveness, frequent dosing is often required to increase the enrichment of copper ions in tumors. However, cuproptosis-mediated tumor therapy lacks high selectivity or intelligence; the accumulation of Cu ions in normal tissues inevitably poses potential safety risks [37]. Therefore, the rational design of a TME-responsive nanoplatform as a copper

ion carrier is crucial for achieving tumor-specific cuproptosis [38, 39]. Moreover, the presence of copper ions in the tumor microenvironment can interfere with the binding of these ions to the lipoylated molecules in the TCA cycle due to the abundance of GSH, potentially diminishing the efficacy of copper-induced toxicity [40, 41]. Thus, on the foundation of achieving tumor-specific cuproptosis, consuming GSH through the modulation of the TME should be overcome to further enhance the cuproptosis effect. To achieve both cuproptosis and GSH depletion, various copper-based nanomaterials with multivalent metal ions have been employed for TME-regulation enhanced cuproptosis and CDT [42–44]. However, the biodegradability characteristics of these copper-based nanomaterials are difficult to control; non-specific degradation cannot achieve tumor-specific cuproptosis, and non-degradable properties greatly limit the therapeutic efficiency of cuproptosis. Consequently, the proper management of the degradation rate of copper carriers is a critical factor in enhancing the effects of cuproptosis, TME regulation, and CDT.

On the other hand, cancer therapies that utilize ROS, such as radiotherapy, photodynamic, and sonodynamic therapy, have the potential to induce ICD effects as well [45–51]. However, as a non-invasive treatment, radiotherapy can treat deep-seated tumors but is associated with significant toxicity, strong side effects, and long treatment cycles [6]. PDT is a minimally invasive treatment that causes less damage to surrounding normal tissues, but its light sources have limited tissue penetration, potentially affecting the treatment of deeper tumors [52, 53]. SDT combines the advantages of PDT and radiotherapy, using ultrasound (US) with deeper penetration depth to activate sonosensitizers [54–56]. Nonetheless, the ability of SDT-induced ICD is greatly hampered by the insufficient generation of ROS as a result of the low efficacy of sonosensitizers and the complicated TME [7, 57], Traditional organic sonosensitizers suffer from poor stability, potential phototoxicity, unstable chemical properties, and inorganic nanomaterials often have wide bandgaps and rapid electron-hole pair recombination, leading to low ROS production rates [58]. Researchers have been investigating the creation of heterojunctions with aligned bandgaps in order to prevent electron-hole pair recombination [59, 60]. Building on this foundation, the development of heterojunction sonosensitizers utilizing copper-based nanomaterials shows potential in regulating the degradation characteristics of copper carriers.

Compared with other Cu-based nanomaterials, such as CuO, CuS, and $CuFe_2O_4$, Cu_2O possesses good sonodynamic and Fenton-like reaction activities owing to the narrow bandgap and the presence of Cu^+ [61]. In addition, Cu_2O holds promise as a copper carrier for cuproptosis, primarily because of its easily degradable nature [42, 62, 63]. Despite being within normal physiological conditions, Cu_2O degradation can still trigger cuproptosis in healthy cells, ultimately causing irreversible harm to normal tissues. In this work, to control the degradation rate of Cu_2O nanocubes, we utilize Cu-MOF formed in-situ as a protection layer to load in Cu_2O to form a Z-scheme heterojunction. The CMC fabricated in-situ not only show improved sonodynamic activity, but also demonstrate controllable degradation behaviors, which are resistant to degradation under normal physiological conditions but can selectively degrade and release copper ions in TME. By releasing Cu^+ and Cu^{2+} specifically in tumors, a cascading amplification of ROS production is achieved. Additionally, the relevance lies in the release of Cu^+, which triggers tumor-specific cuproptosis by stimulating DLAT oligomerization. Due to these favorable properties, CMC heterojunctions significantly enhance a potent ICD effect by boosting ROS levels and inducing tumor-specific cuproptosis (Scheme 1). As a result, primary tumors are completely eliminated, and distant tumors are almost fully suppressed. The exploration of novel therapeutic approaches such as cuproptosis, SDT, CDT, and immunotherapy not only enriches our understanding of cell death mechanisms but also provides new insights for cancer therapy, paving the way for cancer treatment with lower side effects and higher efficiency.

Results and discussion

Synthesis and structural characterization of CMC

We synthesized Cu_2O nanocubes through the mild precipitation method. A reaction took place when copper sulfate was combined with NaOH in the presence of SDS to form $Cu(OH)_2$, which was subsequently reduced to Cu^+ by sodium ascorbate (SA) under room temperature stirring. TEM image revealed regular cubic structures of Cu_2O with a size of about 90 nm (Fig. 1a), similar to the hydrodynamic diameter (112.4 nm) determined by DLS measurements (Fig. 1f). To overcome the susceptibility of Cu_2O nanoparticles to oxidation in practical applications, we combined Cu_2O with 2,3,6,7,10,11-hexahydroxytriphenylene (HHTP) to prepare CMC nanoparticles. TEM images clearly show a distinct core-shell structure formed on the cubic structure of Cu_2O (Fig. 1b), uniformly wrapped by a layer of material about 20 nm thick, with the size of CMC about 130 nm. The hydrodynamic diameter increased from 112.4 nm for Cu_2O to 168.5 nm for CMC (Fig. 1f), similar to the TEM observations, slightly larger than the diameter of the Cu_2O nanocubes. TEM image also demonstrated that the surface coating of Cu-MOF does not affect the original surface morphology of the Cu_2O nanocubes. Furthermore, the mapping of CMC at high magnification were obtained by element mapping to characterize the dispersion of the element distribution of CMC, as shown in Fig. S1, the elements

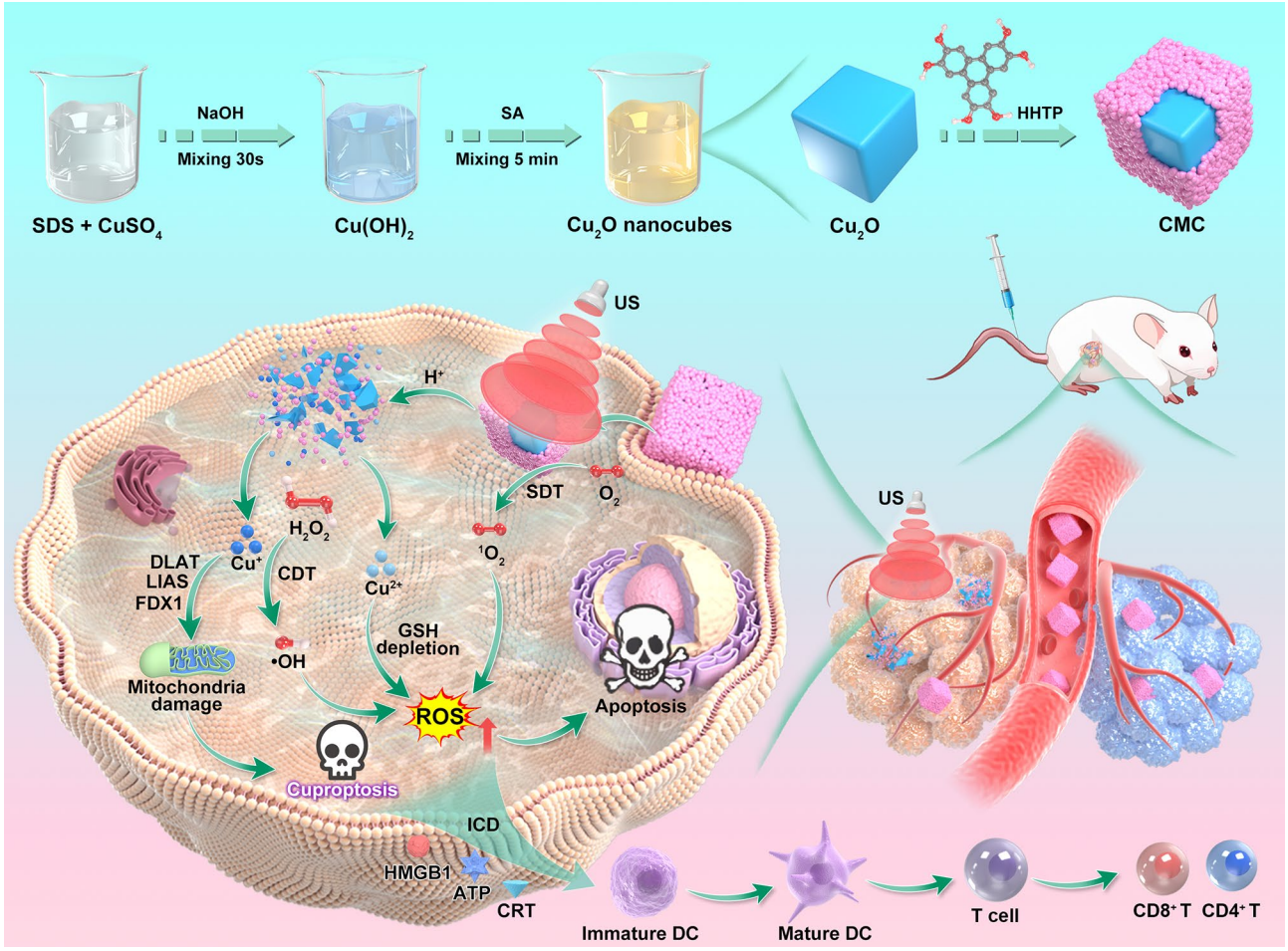

Scheme 1 A scheme to show the preparation of CMC heterojunctions for tumor-specific cuproptosis-enhanced SDT/CDT/immunotherapy

of Cu, O, C and N are successfully distributed in CMC. Figure 1c shows the colors of Cu_2O and CMC at the same concentration, with Cu_2O appearing yellow and CMC dark green, which also confirmed the successful preparation of heterojunctions. Figure 1d illustrates that Cu_2O has a distinct absorption peak at 496 nm, which can also be detected in that of CMC. Furthermore, the absorption intensity of CMC is significantly higher than that of Cu_2O at the same concentration (200 μg/mL). Zeta potential measurements for Cu_2O and CMC were 23.1 ± 1.8 and 39.3 ± 3.07 mV, respectively (Fig. 1e).

Next, the chemical composition of Cu_2O and CMC was studied through a series of characterizations such as XRD and XPS. The successful synthesis of Cu_2O and CMC was confirmed by their XRD patterns (Fig. 1g, h), which correspond to the Cu_2O nanostructure (PDF#99 – 0041). In the XRD spectrum of Cu_2O, distinct diffraction peaks are observed at ~ 29.5°, ~ 36.4°, ~ 42.3°, ~ 61.4°, and ~ 73.6°, corresponding to the (110), (111), (200), (220), (220), and (311) crystal planes of Cu_2O, respectively. Notably, no impurity peaks were observed, indicating that the synthesized Cu_2O possesses good crystalline and purity. For CMC, the characteristic diffraction peaks of Cu_2O are clear, but there are no distinct Cu-MOF diffraction peaks, and the corresponding XRD diffraction peaks are weaker compared to Cu_2O. This weakening could be due to the low intensity of Cu-MOF's diffraction peaks and the fact that Cu-MOF encapsulation diminishes the intensity of Cu_2O's diffraction peaks. XPS was utilized to analyze the valence states and composition of the different samples (Fig. 1i, m). The Cu_2O's peaks in high-resolution Cu 2p spectrum at ~ 931.9, ~ 933.9, ~ 951.8, and ~ 953.9 eV was observed (Fig. 1k). The results for CMC are similar to those of Cu_2O, with peaks at ~ 932.0, ~ 932.7, ~ 951.8, and ~ 953.6 eV (Fig. 1o). Moreover, the ratio of Cu^+ to Cu^{2+} in CMC is much higher than in Cu_2O, with a ratio of 10.11 compared to only 3.85 in Cu_2O, indicating that the encapsulation by Cu-MOF reduces the loss of Cu^+ and enhances the stability of Cu_2O nanocubes. Both CMC and Cu_2O exhibit characteristic C peaks of C-C and C-OH in their high-resolution C 1s spectra (Fig. 1j, n), and typical features of O-H and Cu-O in their high-resolution O 1s spectra (Fig. 1l, p). These above structural characterization results clearly demonstrate the

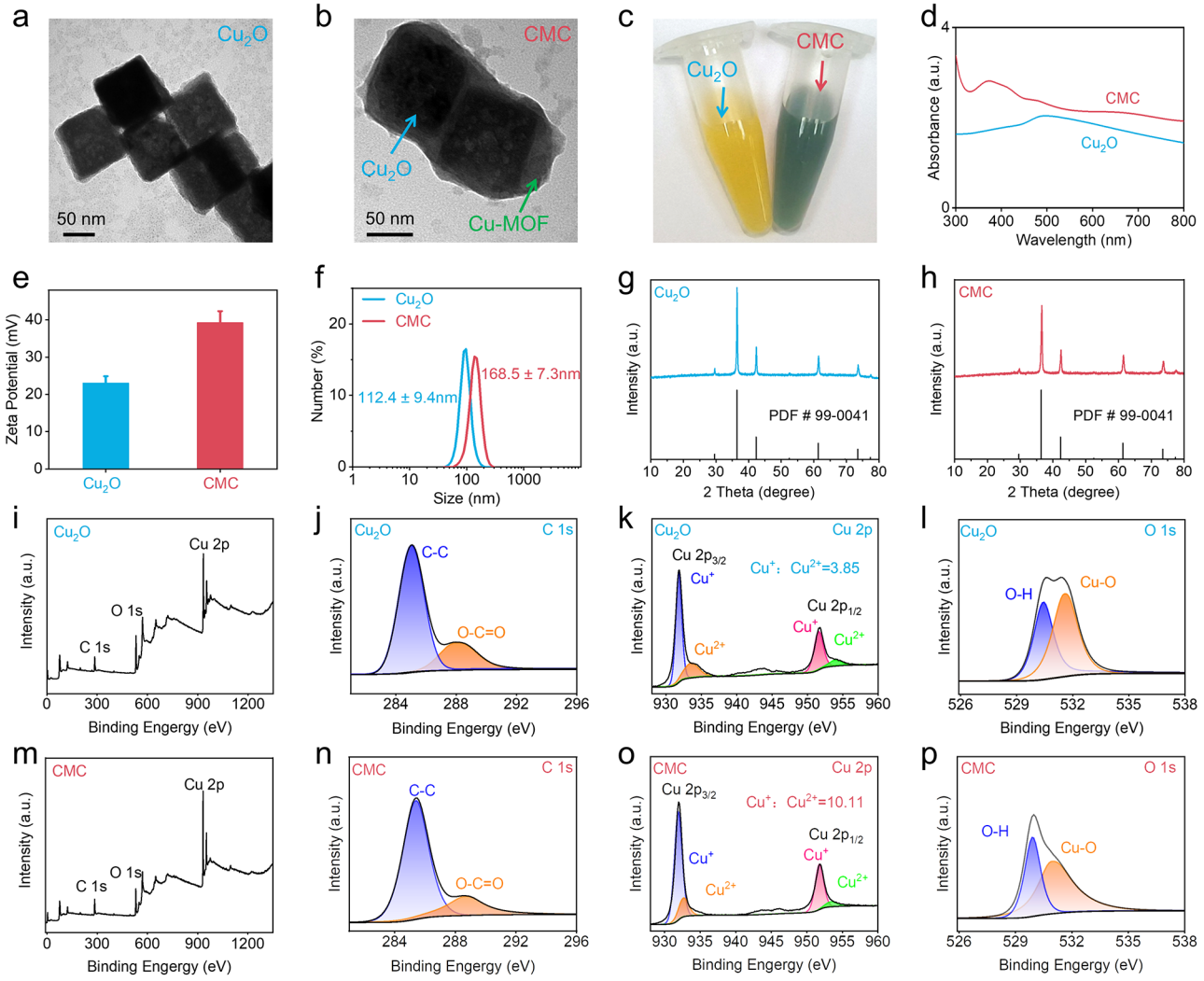

Fig. 1 Characterization of CMC. (**a**, **b**) TEM images of Cu_2O and CMC. (**c**) Photographic images displaying the colors of Cu_2O (yellow) and CMC (dark green) at the same concentration. (**d-f**) UV-visible absorption spectra, Zeta potential ($n = 3$), and hydrodynamic diameters of Cu_2O and CMC ($n = 3$). (**g**, **h**) XRD spectra of Cu_2O and CMC. (**i-p**) XPS spectra of Cu_2O and CMC, including measurements of survey XPS, high-resolution C 1s, Cu 2p, and O 1s spectra

successful preparation of Cu_2O nanocubes and CMC heterojunctions.

Heterojunction-enhanced SDT and CDT performances

Following the successful construction of heterojunctions, we used DPBF as a ROS probe to assess the enhanced sonodynamic characteristics of CMC. As shown in Fig. 2a, b, with the increase in US time (0–10 min), the absorption of DPBF at 418 nm rapidly decreased, indicating significant ROS generation. Under the same conditions, the rate of ROS generation was stronger in the CMC group compared to the single-component Cu_2O group. Specifically, the rate of ROS generation under CMC was 0.15 min^{-1}, 1.5 times that of Cu_2O (0.1 min^{-1}) (Fig. 2c), which robustly validates the superior sonodynamic performance of CMC over pure Cu_2O. The exceptional rate of ROS generation by CMC suggests that the construction of the heterojunction significantly enhances the SDT performance of Cu_2O nanocubes. Since DPBF can detect both $^1O_2$ and $O_2^{-\bullet}$, we used dihydrorhodamine 123 (DHR123) to monitor the $O_2^{-\bullet}$ production capacity of Cu_2O and CMC under US irradiation. The significantly increased fluorescence intensity of DHR123 was observed in Cu_2O and CMC groups under US irradiation (Fig. S2), suggesting their efficient $O_2^{-\bullet}$ generation ability. In addition to $O_2^{-\bullet}$, the generation of $^1O_2$ by CMC under US irradiation was confirmed by the ESR spectra. As shown in Fig. S3, both Cu_2O and CMC exhibited the significant ESR signal, indicating the generation of $^1O_2$. Therefore, CMC-mediated ROS generation involves both energy transfer and electron transfer processes, producing $^1O_2$ and $O_2^{-\bullet}$ simultaneously.

Next, by analyzing the bandgap structures of Cu_2O and Cu-MOF, we explored the mechanism behind the

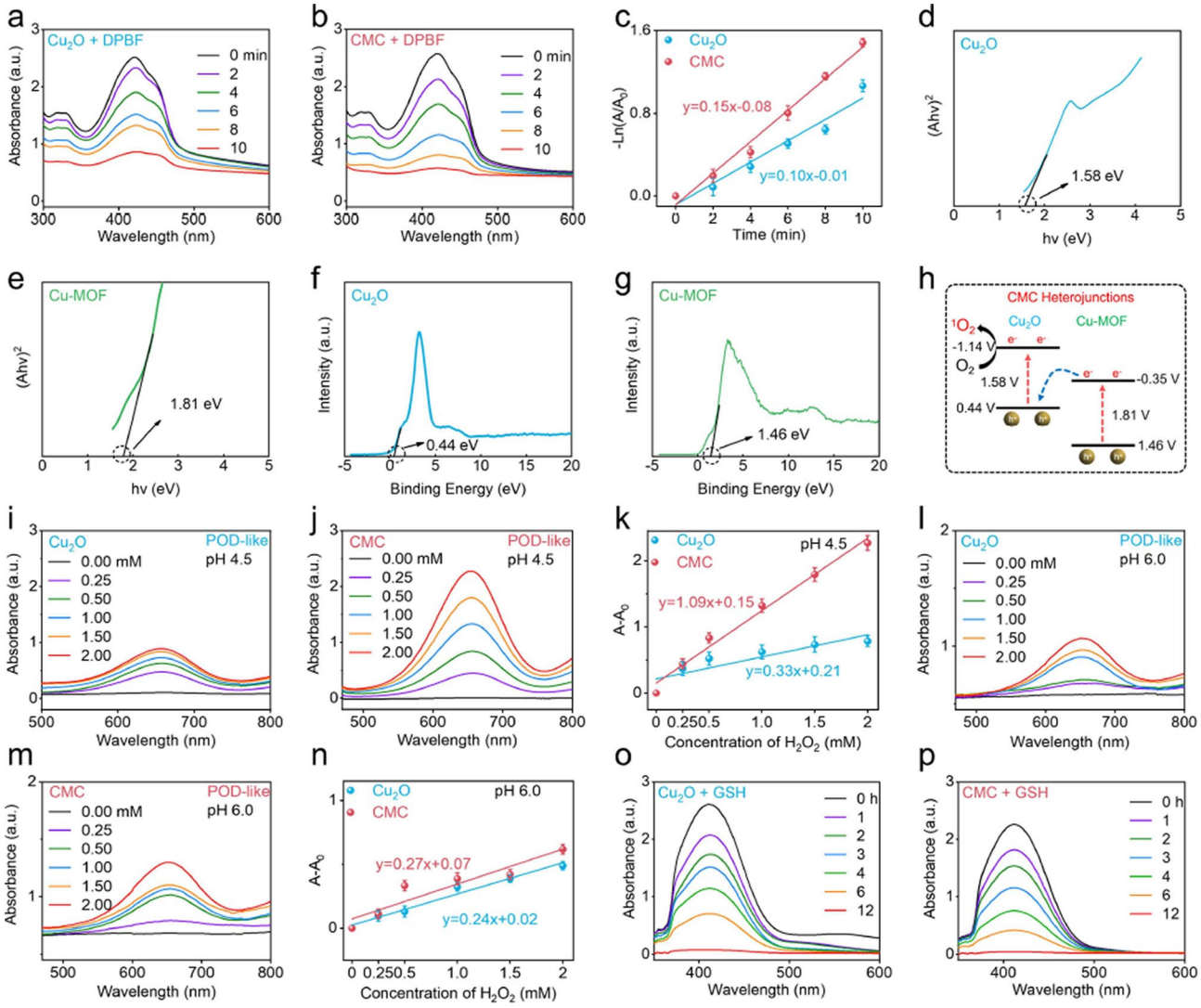

Fig. 2 Heterojunction-enhanced SDT and CDT performances. (**a**, **b**) Evaluation of $^1O_2$ generation efficiency of Cu_2O and CMC under US irradiation. (**c**) Comparison of the rate constants for $^1O_2$ generation triggered by US in the presence of Cu_2O and CMC ($n = 3$). (**d-g**) Tauc plots and XPS-VB spectra of Cu_2O and CMC. (**h**) Energy band diagrams of Cu_2O and CMC. (**i**, **j**) Generation of •OH by Cu_2O and CMC at pH 4.5. (**k**) Comparison of the chemodynamic effects of Cu_2O and CMC at pH 4.5 ($n = 3$). (**l**, **m**) Generation of •OH by Cu_2O and CMC in the presence of hydrogen peroxide at pH 6.0. (**n**) Comparison of the chemodynamic effects of Cu_2O and CMC at pH 6.0 ($n = 3$). (**o**, **p**) Evaluation of GSH depletion by Cu_2O and CMC. The concentration of Cu_2O and CMC was 200 μg/mL

enhanced sonodynamic activity of CMC. Initially, the valence bands (VB) of Cu_2O and Cu-MOF were determined using XPS-VB spectroscopy, which were found to be 0.44 eV and 1.46 eV respectively (Fig. 2f, g). Subsequently, the corresponding standard hydrogen electrode ($E_{VB,\ NHE}$) values were calculated. The $E_{VB,\ NHE}$ for Cu_2O and Cu-MOF were calculated as 0.44 eV and 1.46 eV, respectively. The bandgaps (E_{BG}) of Cu_2O and Cu-MOF were obtained from Tauc plots derived from UV-vis spectroscopy, which determined the bandgaps to be 1.58 eV and 1.81 eV, respectively (Fig. 2d, e). Based on $E_{VB} = E_{CB} + E_{BG}$, the conduction bands (CBs) of Cu_2O and Cu-MOF were calculated as -1.14 eV and − 0.35 eV, respectively. From these measurements, we plotted the energy band diagrams of Cu_2O and Cu-MOF (Fig. 2h). Therefore, the electron transfer occurs from the conduction band of Cu-MOF to the valence band of Cu_2O. CMC's enhanced sonodynamic performance is likely attributed to the development of a Z-type heterojunction, which hinders the recombination of electron-hole pairs within the separate semiconductors. Therefore, the improved sonodynamic performance of the CMC heterostructure can be attributed to its efficient electron-hole separation efficiency.

Due to the rich presence of Cu^+ in CMC, we then measured its chemodynamic performance under different pH using TMB as a probe. By monitoring changes in absorbance at 652 nm, the capacity of CMC and Cu_2O

to generate •OH was assessed. At a low pH of 4.5, the absorption peaks at 652 nm for both Cu_2O and CMC increased with the concentration of hydrogen peroxide (Fig. 2i, j). CMC demonstrated significantly higher •OH generation efficiency compared to Cu_2O, with a rate of 1.09 min^{-1} (Fig. 2k) versus 0.33 min^{-1} for Cu_2O. The enhanced CDT performance can be attributed to accelerated electron transfer processes within the CMC heterostructure. At pH 6.0, the CDT properties of CMC were also studied (Fig. 2l-n), where CMC still showed a higher •OH generation rate (0.27 min^{-1}) compared to Cu_2O (0.24 min^{-1}). We also calculated the V_{max} and K_m of Cu_2O and CMC using Michaelis-Menten kinetic analysis. As depicted in Fig. S4, the higher V_{max} and the lower K_m can be detected in the CMC group compared with that in the Cu_2O group at pH 4.5 and 6.0, indicating the higher chemodynamic activity of CMC. However, the •OH generation rates for both CMC and Cu_2O decreased compared to those at pH 4.5. Importantly, at pH 7.4, Cu_2O still showed Fenton-like reaction activity and •OH production ability (Fig. S5a), indicating that Cu_2O could be degraded under normal physiological conditions to release Cu^+ for triggering CDT effect. For comparison, almost no •OH generation was observed for CMC at pH 7.4 (Fig. S5b), suggesting that the coating of Cu-MOF could regulate the degradation behaviors of Cu_2O nanocubes to avoid the CDT in normal cells.

To verify that the composite material we constructed has excellent SDT and CDT properties because of the formation of a heterojunction, rather than simply mixing the two materials. We prepared a physical mixture of Cu_2O and Cu-MOF, which was then compared with CMC. As depicted in Fig. S6, the $^1O_2$ and •OH generation efficiency of CMC was significantly higher than the physical mixture of Cu_2O and Cu-MOF. These results forcefully demonstrated that the enhanced SDT/CDT performance of CMC could be ascribed to the formation of Z-scheme heterojunctions rather than the physical mixture of Cu_2O and Cu-MOF.

Given the abundance of GSH in the TME, the ROS ($^1O_2$ and •OH) created by the SDT-CDT combination could be counteracted by GSH, thus decreasing the therapeutic impact of SDT and CDT. Given the presence of Cu^{2+} in CMC, we further assessed its capacity for GSH depletion. Using DTNB as a probe, the reaction between CMC and GSH was monitored. As shown in Fig. 2p, o, the absorption peak at 412 nm for CMC or Cu_2O alone decreased sharply within 12 h, indicating a strong GSH depletion capability. By significantly enhancing GSH depletion, CMC successfully tackled GSH-mediated resistance in the tumor microenvironment, ultimately boosting the therapeutic impact of CDT-SDT in tumor treatment.

pH-responsive biodegradation behavior of CMC

After demonstrating the heterojunction-enhanced SDT and CDT performances of CMC, we then studied their biodegradability through dialysis. During dialysis, degradation of Cu_2O was observed as early as 20 min (Fig. S7a), with rapid degradation progressing to a translucent light yellow by 40 min. And it approaches a nearly transparent colorless state by 90 min. CMC, however, remained stable during the first two days, potentially providing a stable window for SDT (Fig. S7b). After two days, the composite material began to degrade, turning from dark green to dark blue by the third day, likely due to the degradation of the Cu_2O encapsulated within CMC. By the fifth day, CMC had turned to a translucent blue. UV-vis absorption spectra at various time points, as shown in Fig. 3e, f, further indicate that the absorption of Cu_2O and CMC gradually decreased with the duration of dialysis, and the corresponding absorption curves tended to flatten by the end of dialysis.

For a more comprehensive view of the degradation process of CMC, TEM images were acquired on 1, 3, and 5 days (Fig. 3b-d). On the first day, the morphology of CMC remained unchanged, by the third day, CMC showed overall aggregation, but separation between Cu-MOF and Cu_2O began to occur. On the fifth day, Cu_2O was almost completely invisible. TEM images were also obtained for Cu_2O during corresponding stages of degradation (20, 40, 90 min) (Fig. 3a and S8), where by 40 min Cu_2O had diminished in size and showed significant aggregation, unable to maintain its stable cubic structure, and by 90 min it was almost completely degraded. These results demonstrate that the coating of Cu-MOF on the surface of Cu_2O could mitigate the degradation process of Cu_2O under the acidic conditions.

We then evaluated the sonodynamic performance of CMC during its degradation. The presence of Cu-MOF plays a crucial role in enhancing SDT performance, allowing CMC to remain stable for a certain period. One day after dialysis began, it still demonstrated good $^1O_2$ generation capabilities of CMC (Fig. 3i), whereas Cu_2O showed significantly reduced $^1O_2$ generating ability just 20 min into dialysis (Fig. 3g). By the end of the dialysis process for both Cu_2O and CMC, there was no remaining SDT activity (Fig. 3h, j). These results demonstrate that CMC significantly improves the stability of Cu_2O nanocubes and confirm that the ROS generation function activated by US through CMC can be sustained within a stable one-day window.

The structural characterization of CMC and Cu_2O was performed to unveil their degradation mechanism including XRD patterns and XPS spectra. The XRD patterns of Cu_2O and CMC at their respective dialysis points were measured. The diffraction peaks for Cu_2O after 90 min of dialysis and for CMC after five days of

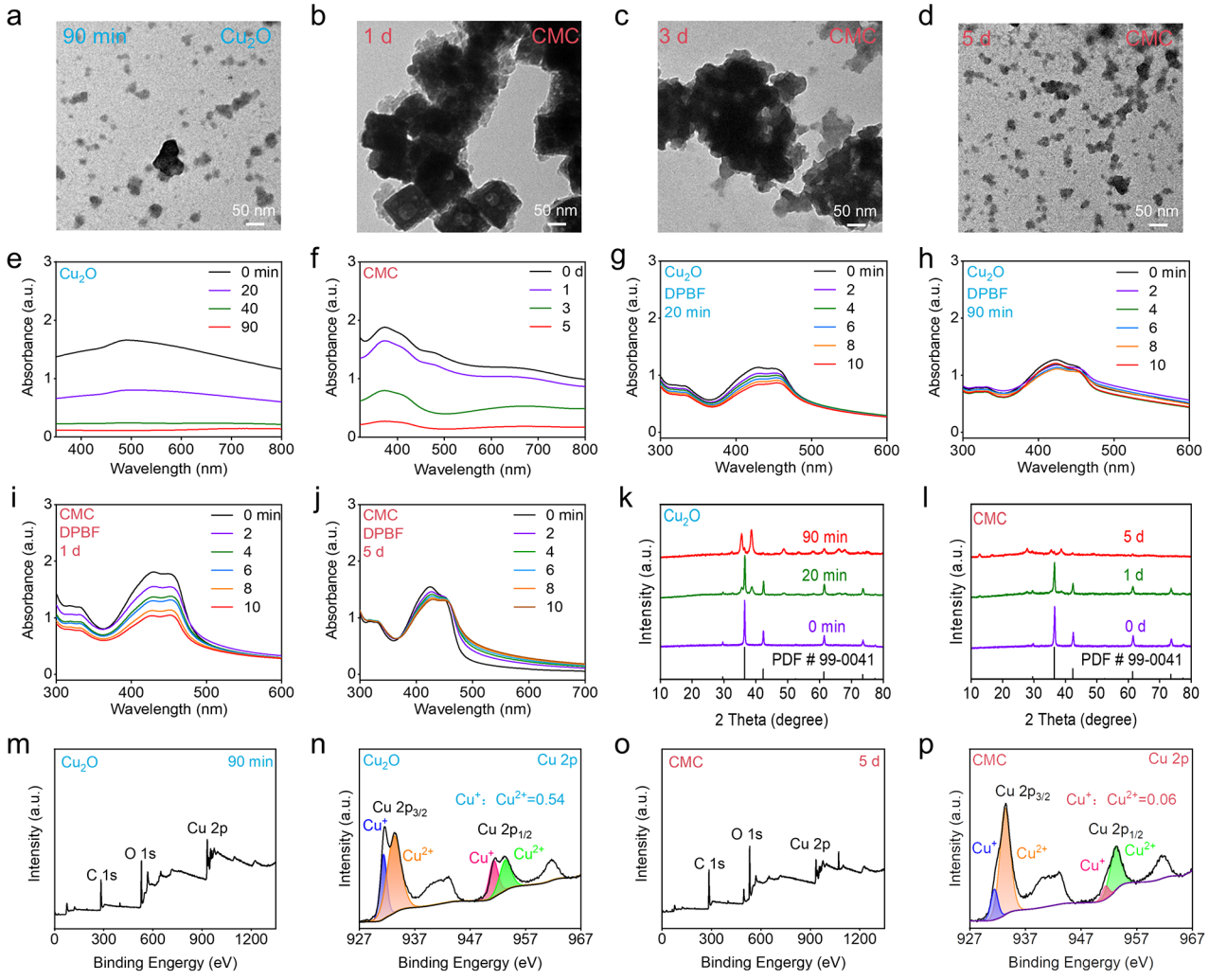

Fig. 3 pH-responsive biodegradation behavior of CMC. (**a-d**) Morphological changes in CMC and Cu_2O with extended exposure time at pH 6.0. (**e**, **f**) UV-vis absorption spectra of Cu_2O and CMC at pH 6.0 after incubation of different times. (**g-j**) Evaluation of $^1O_2$ generation capability of Cu_2O and CMC at pH 6.0 after incubation of different times. (**k**, **l**) XRD patterns of Cu_2O and CMC after degradation at pH 6.0 for different times. (**m-p**) The survey XPS and high-resolution Cu 2p spectra of Cu_2O and CMC after degradation at pH 6.0 for different times

dialysis were weakened or almost disappeared (Fig. 3k, l). Furthermore, high-resolution Cu 2p XPS spectra were measured to detect changes in the Cu^+/Cu^{2+} ratio after 90 min of dialysis for Cu_2O and five days for CMC (Fig. 3m-p). The Cu^+/Cu^{2+} ratio for Cu_2O decreased from 3.85 to 0.54 after 90 min of dialysis, and for CMC it dropped from 10.11 to 0.06 after five days, indicating that nearly all Cu^+ in Cu_2O and CMC had been oxidized to Cu^{2+}. These results indicate that the degradation mechanism of CMC and Cu_2O was ascribed to the oxidation of Cu^+ to Cu^{2+}.

Similar to pH 6.0, the noticeably lightened color of Cu_2O solution can be detected after 4 h at pH 7.4 (Fig. S9a), suggesting that Cu_2O can deteriorate in the acidic and normal physiological condition. After Cu-MOF coating, insignificant change of the absorption spectrum of CMC heterojunctions can be detected after storing for 5 days at pH 7.4 (Fig. S9d), illustrating that CMC cannot be degraded in normal physiological conditions. Furthermore, as presented in Fig. S9b, no obvious color change can be observed in CMC solution after storing for 5 days at pH 7.4. This not only limits its ability to successfully conduct SDT/CDT, but also brings about harmful consequences on normal tissues. The Cu-MOF coating functions as a protective barrier, stopping the non-specific degradation of Cu_2O nanocubes on normal tissues and enabling the specific induction of cuproptosis and CDT in tumors.

In vitro antitumor efficacy of CMC

After confirming the enhanced sonodynamic and chemodynamic properties of CMC, we investigated its synergistic tumor treatment effects at the cellular level. Initially, we used confocal imaging microscopy to study the uptake behavior of CMC and Cu_2O in 4T1 cells. Cu_2O and CMC were

labeled with FITC fluorescent dyes to evaluate their cellular uptake. The fluorescence imaging showed bright green fluorescence in the cytoplasm of 4T1 cells, indicating effective intracellular uptake of Cu_2O and CMC (Fig. S10). Next, we assessed the biocompatibility of CMC and Cu_2O. As shown in Fig. S11, LO2 cells treated with different concentrations of Cu_2O for 24–48 h exhibited significant cytotoxicity, indicating that Cu_2O can degrade in the normal physiological conditions to release Cu^+. Conversely, CMC did not exhibit any notable cytotoxicity towards LO2 cells, as shown in Fig. S12. This indicates that the Cu-MOF coating effectively protects Cu_2O nanocubes from degradation in normal cells. The CCK-8 results presented in Fig. 4a-d showed the cell viability of 4T1 cells after different treatments for 24 and 48 h. Compared with the single-component Cu_2O nanocubes, CMC exhibited higher cytotoxicity against 4T1 cells at the same conditions, which could be ascribed to the stronger chemodynamic activity of heterojunctions. Moreover, the severe cell death phenomenon of 4T1 cells treated with CMC in the presence of US irradiation was observed (Fig. 4d). The cytotoxicity of CMC + US against 4T1 cells was much higher than that of the single-component Cu_2O nanocubes (Fig. 4c).

The superior therapeutic effect of CMC through SDT and CDT was further evaluated using live/dead cell staining. As shown in Fig. 4e, no red fluorescence signals were detected in the control and US alone groups, indicating that US (50 kHz, 1.0 Wcm^{-2}) alone does not have significant cytotoxicity. Both Cu_2O and CMC alone groups showed decreased green fluorescence signals and increased red fluorescence signals, verifying their good chemodynamic effects. Furthermore, the red fluorescence intensity in the CMC group was higher than that in the Cu_2O alone group (Fig. S13a), confirming the enhanced chemodynamic activity of heterojunctions. The CMC + US group exhibited significantly higher red fluorescence signals than the Cu_2O + US group, demonstrating the synergistic enhancement between CDT and SDT. These results clearly indicated that the construction of CMC heterojunctions greatly improved the efficiency of SDT and CDT treatment through Cu_2O alone.

We then investigated the antitumor mechanism of CMC-mediated SDT and CDT. The intracellular ROS levels induced by CMC + US were determined using DCFH-DA as the ROS probe. There were no significant ROS fluorescence signals in the control and US alone groups of 4T1 cells (Fig. 4f), suggesting that the US alone could not generate ROS to induce apoptosis. In contrast, the CMC alone and Cu_2O alone groups exhibited a bright ROS fluorescence signal, confirming the enhanced intracellular ROS generation by CMC and Cu_2O. Notably, the highest ROS signal can be detected in the CMC + US group (Fig. S13b), demonstrating the high-efficiency sonodynamic and chemodynamic activities of heterojunctions.

In vitro antitumor mechanism of CMC

In addition to ROS-mediated antitumor mechanism, we then investigated the cuproptosis-mediated antitumor mechanism owing to the presence of Cu^+ in CMC. Cuproptosis is known to be especially potent against cancer cells that have strong mitochondrial respiration, such as 4T1 cells [62]. Consequently, we opted for 4T1 cells as the subject of our study to assess the impact of CMC on the cuproptosis pathway. As presented in Fig. 5a, both Cu_2O and CMC treatments led to significant oligomerization of lipoylated DLAT, confirming that Cu_2O and CMC induced cuproptosis, likely promoting the aggregation of lipoylated proteins. Additionally, Cu_2O and CMC treatments reduced the levels of FDX1 and LIAS (Fig. S14), with the CMC treatment group showing a more pronounced decrease in FDX1 and LIAS levels compared to the Cu_2O treatment group. Pyruvate, the starting substrate of the TCA cycle, reflects the efficiency of the TCA cycle [64]. As shown in Fig. 5d, the highest levels of pyruvate content can be observed in the CMC + US treatment group, demonstrating that copper ions affects components of the TCA cycle, inhibits the cycle and leads to pyruvate accumulation.

We then examined the morphological changes in mitochondria after copper ion uptake. Bio-TEM analysis showed significant disruption of mitochondrial structures in 4T1 cells treated with CMC (Fig. 5c). Compared to the control group (Fig. 5b), the CMC-treated 4T1 cells exhibited reduced inner mitochondrial membranes and large vacuoles, further confirming that 4T1 cells treated with CMC underwent cuproptosis. The JC-1 mitochondrial membrane potential staining assay was used to detect the disruptive effects of CMC on mitochondria. Following copper ion treatment, the Cu_2O and CMC alone groups showed a reduction in red fluorescence signals and an elevation in green fluorescence signals (Fig. 5e). The increase in green fluorescence signal in the JC-1 assay for the CMC + US group was significantly higher than that of the Cu_2O + US group (Fig. S13c). This phenomenon demonstrated that copper-induced cell death is related to mitochondrial metabolism and that US further promotes mitochondrial metabolism, clearly confirming that the preparation of CMC greatly enhances the synergistic effects of copper-induced cell death and SDT.

In vitro induction of ICD effects by CMC

After demonstrating the effective in vitro therapeutic effects of CMC through ROS generation and cuproptosis effect, we further investigated the cell death pathways involved in the synergistic action of CDT, SDT and cuproptosis. ROS and cuproptosis have the ability to induce immunogenic cell death in tumor cells, leading to the presentation of CRT, the release of HMGB1 and ATP [65–67]. Dendritic cells can be recruited and activated

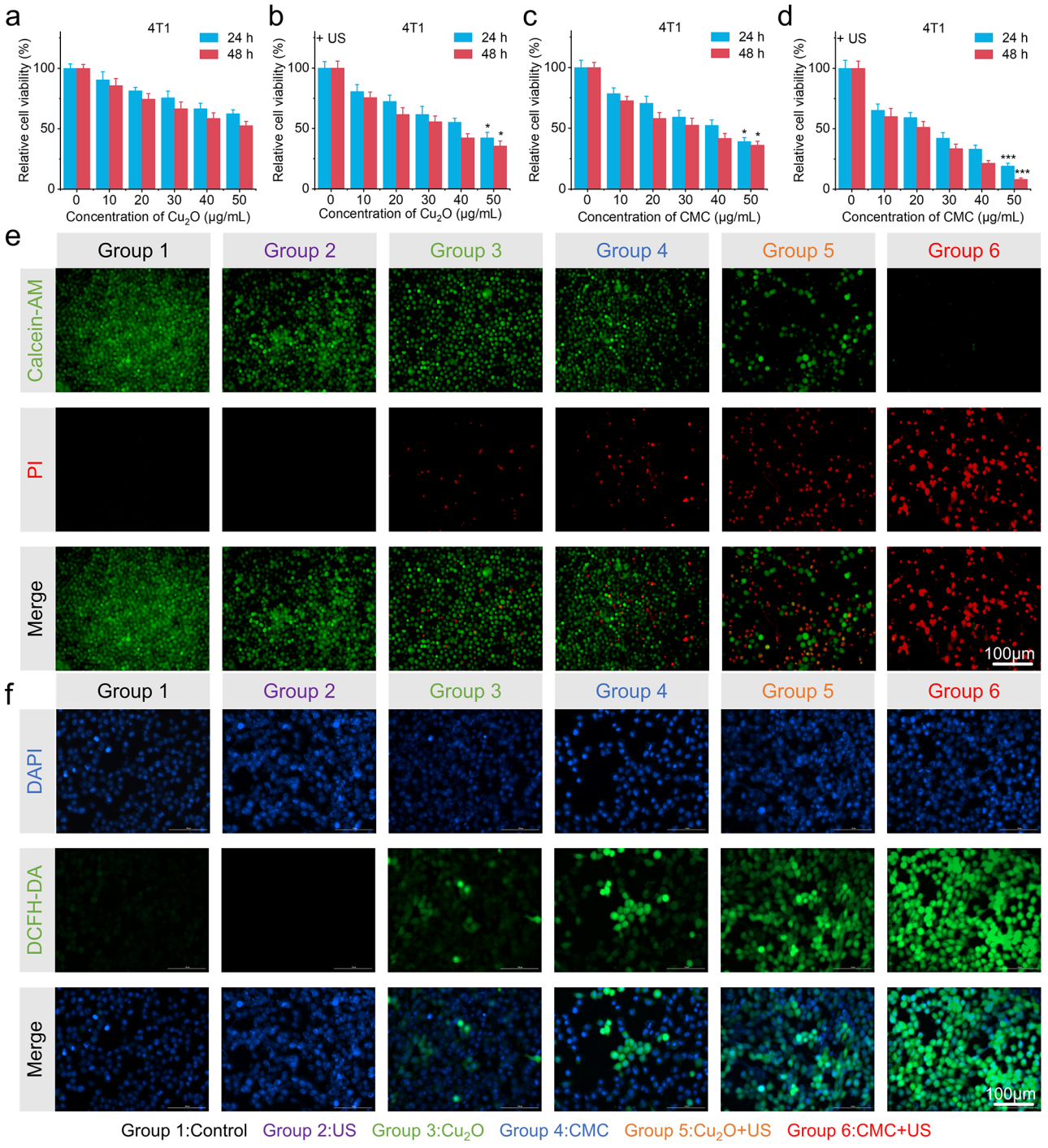

Fig. 4 In vitro antitumor efficacy of CMC. (**a-d**) The relative cell viability of 4T1 cells is assessed after incubation with Cu_2O and CMC, with or without US irradiation. (**e**, **f**) Following different treatments, live/dead cell and ROS staining of 4T1 cells was carried out. Data are presented as the mean ± SD ($n = 6$ and $^*p < 0.05$, $^{***}p < 0.001$)

by these three DAMPs, subsequently initiating an adaptive immune response to eliminate tumor cells [8, 68]. The strongest red fluorescence signal was observed in the CMC + US group compared to other groups (Fig. 6a), indicating that CRT was exposed from the endoplasmic reticulum to the cell surface after the synergistic action of CDT, SDT, and cuproptosis. Next, the highest concentration of HMGB1 was released by 4T1 cells treated with CMC + US (41.5 ± 5.3 μg/ml) compared with the other groups (Fig. 6e). The other groups followed in order: Cu_2O + US (31.2 ± 4.5 μg/ml), CMC (25.5 ± 4.0 μg/ml), and Cu_2O (20.5 ± 3.5 μg/ml). The control group and the

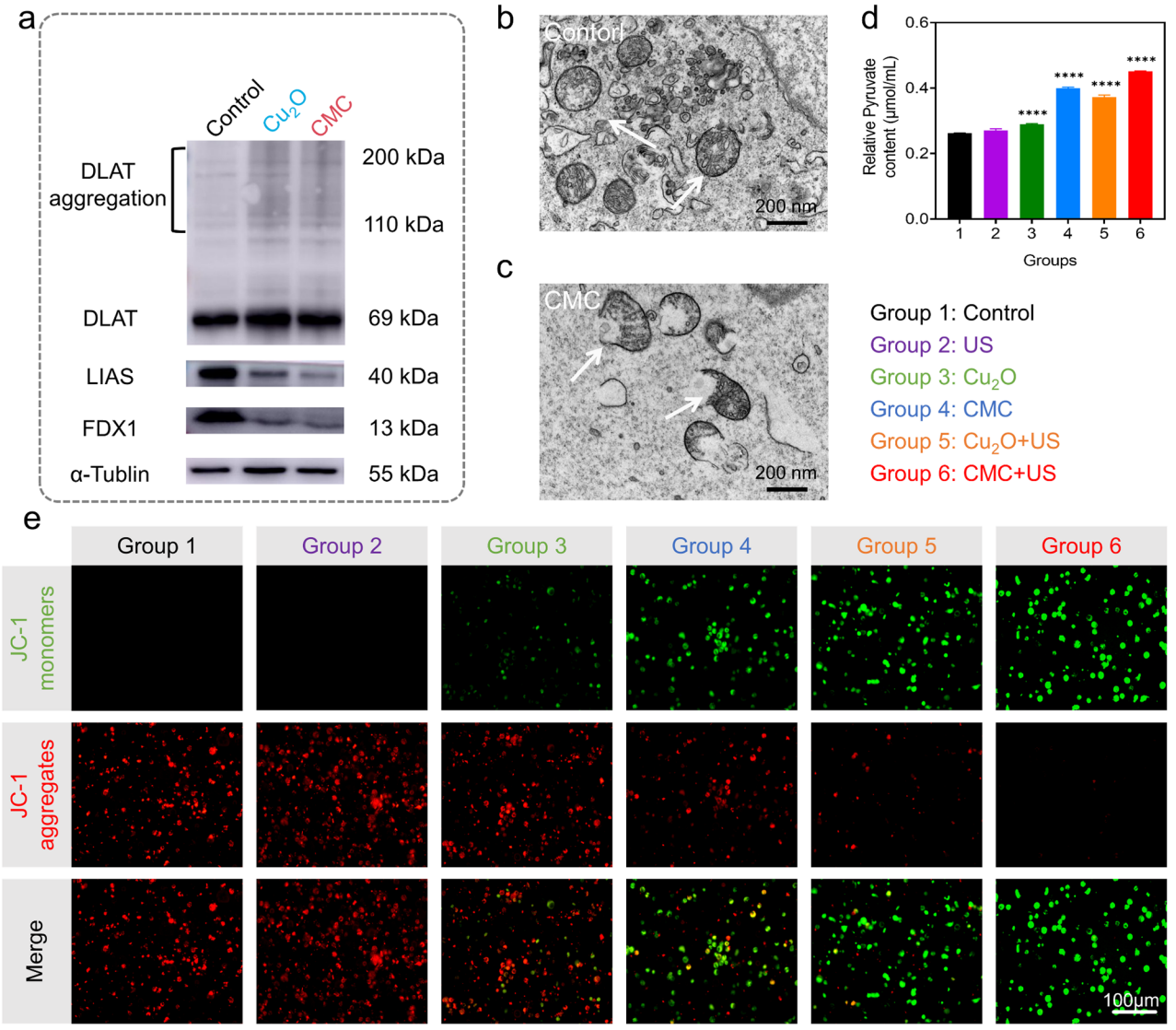

Fig. 5 In vitro antitumor mechanism of CMC. (**a**) Evaluation of DLAT, LIAS, and FDX1 expression in 4T1 cells after different treatments. (**b**, **c**) TEM observations of mitochondrial morphological changes after different treatments. (**d**) Pyruvate content in 4T1 cells after different treatments. (**e**) Fluorescence imaging of mitochondrial membrane potential in 4T1 cells. ($n = 3$ and $^{****}p < 0.0001$)

US alone group showed little difference, with levels of 10.8 ± 1.3 μg/ml and 11.0 ± 1.3 μg/ml, respectively. To further confirm ROS- and cuproptosis-triggered ICD effect, we used an ATP assay kit to evaluate ATP release level in 4T1 cells after different treatments. Figure 6f shows that intracellular ATP levels decreased in the CMC + US group, indicating that CMC could secrete more ATP from the intracellular to the extracellular space under US irradiation. These above results strongly demonstrated that CMC can trigger ICD effect through the synergistic action of CDT, SDT, and cuproptosis. Tumor-associated antigens have the potential to activate DCs, which are an essential type of APCs [45, 69–71]. After adding the supernatant from 4T1 cells co-incubated with CMC (Fig. 6b), the expression levels of CD80 and CD86 on DCs cells were detected. As shown in Fig. 6c, d, CMC + US group exhibited the higher proportion of $CD80^+CD86^+$ DCs compared with the Cu_2O + US group, suggesting that the construction of heterojunctions could enhance the sonodynamic and chemodynamic properties of Cu_2O nanocubes to induce the stronger ICD effects.

In vivo antitumor efficacy of CMC

Considering that the tumor-specific cuproptosis and ROS could induce antitumor immune responses by activating ICD effect, we then investigated the in vivo anticancer effects of CMC. Upon injecting ICG-labeled CMC intravenously, the tumor site exhibited prominent fluorescence signals (Fig. 7b and S15), indicating the gradual accumulation of CMC in the tumor tissue. Furthermore,

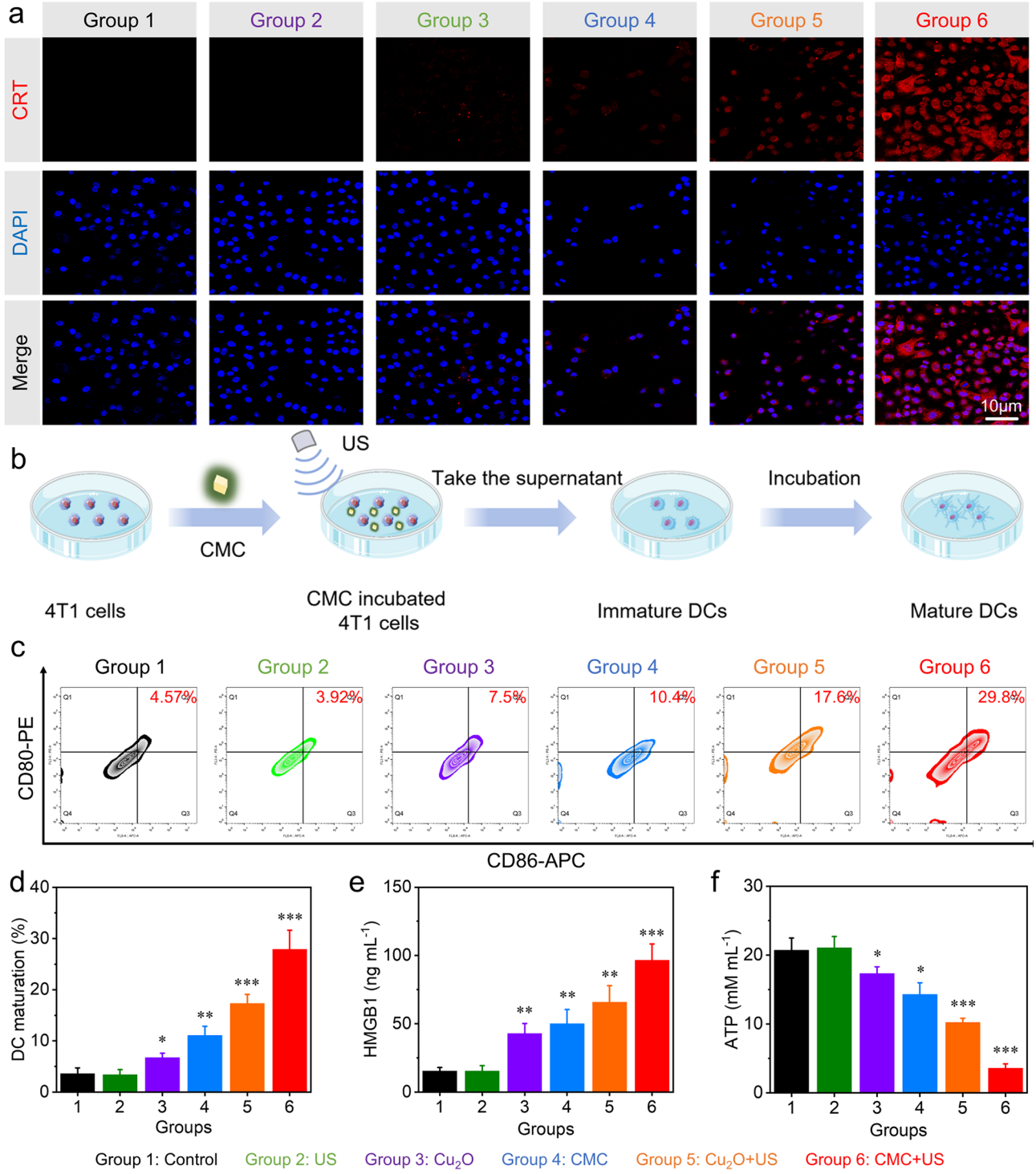

Fig. 6 In vitro induction of ICD effects by CMC. (**a**) Confocal images of CRT exposure in 4T1 cells after different treatments. (**b**) Schematic diagram of the experimental process for CMC activation of DCs. (**c**, **d**) Flow cytometry analysis and corresponding quantitative results of CD80 and CD86 expression in DCs after different treatments. (**e**, **f**) Extracellular HMGB1 levels and Intracellular ATP levels in 4T1 cells after different treatments. ($n = 3$ and $^{*}p < 0.05$, $^{**}p < 0.01$, $^{***}p < 0.001$)

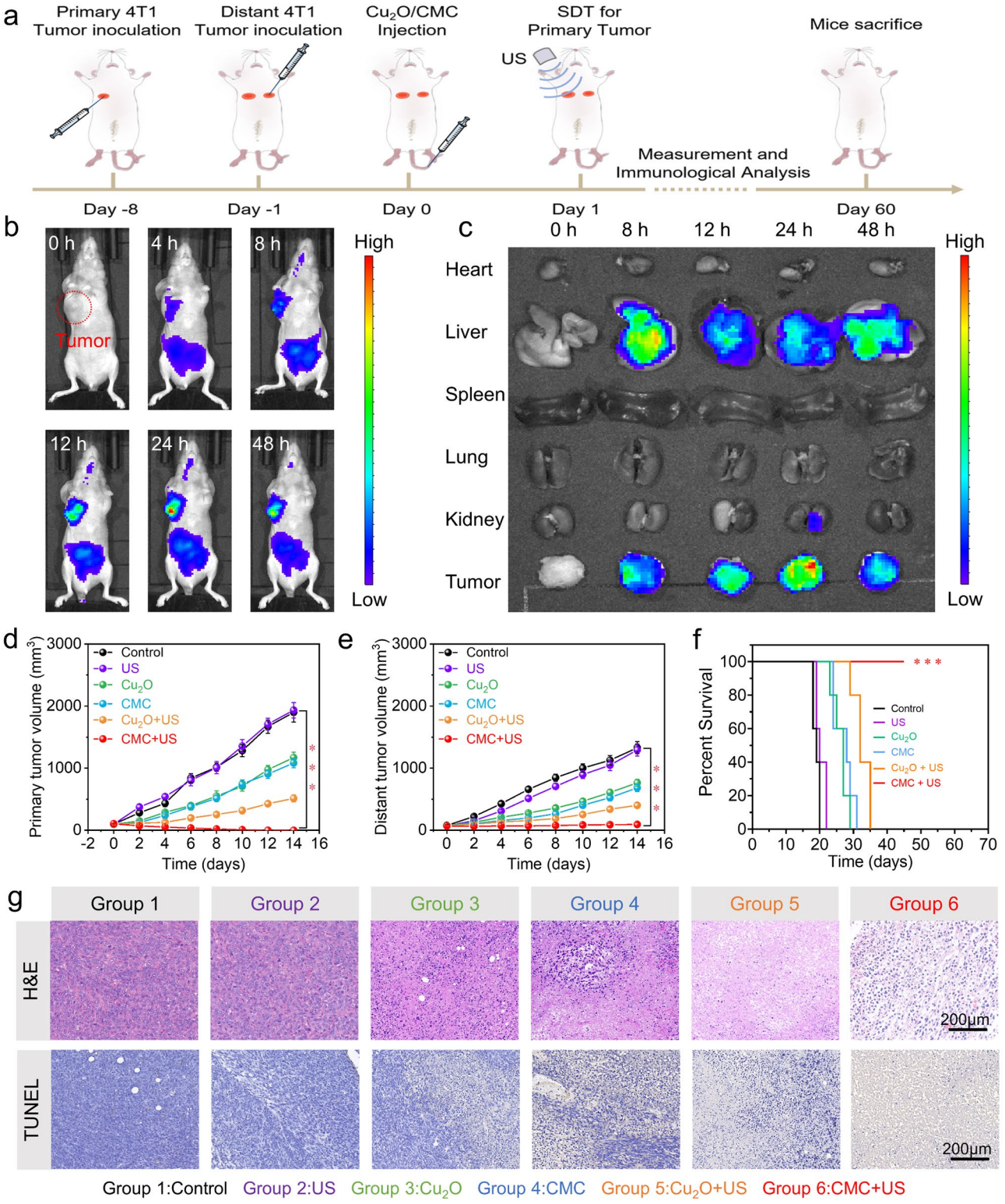

Fig. 7 In vivo antitumor efficacy of CMC. (**a**) In vitro anticancer therapy procedures of CMC are illustrated schematically. (**b**, **c**) In vivo and ex vivo NIR imaging of CMC. (**d**, **e**) Tumor growth curves of primary (**d**) and distant tumors (**e**) in different treatment groups of mice. (**f**) Survival rates of mice in different treatment groups. (**g**) H&E and TUNEL staining of primary tumors after different treatments. ($n = 3$ and $^{***}p < 0.001$)

the ex vivo NIR imaging results showed that CMC accumulation in the tumor tissue was highest 24 h after injection (Fig. 7c and S16). On this basis, US irradiation should be performed 24 h after intravenous injection of CMC.

Considering that treating the primary tumor can activate the immune system, we constructed a bilateral tumor model to evaluate whether CMC-mediated immunotherapy can inhibit the growth of distant tumors. During the treatment, neither the control group nor the US group showed significant inhibition of primary or distant tumor growth. In the Cu_2O and CMC groups, tumor volume growth in both primary and distant tumors was reduced compared to the control or US groups (Fig. 7d, e), indicating that CMC-induced CDT and cuproptosis had a certain therapeutic effect within the TME. Compared to the Cu_2O + US group, the CMC + US group exhibited greater inhibition of tumor growth, demonstrating enhanced synergistic therapeutic effects of CDT, SDT, and tumor-specific cuproptosis. In addition, it is worth noting that the primary tumors in the CMC + US group were completely eliminated within a mere 8 days, underscoring the formidable antitumor capabilities of CMC. The growth of distant tumors in CMC + US group was almost completely inhibited, which was superior to that in CMC alone group. Additionally, mice in the CMC + US group survived for 45 days, while mice in the control group survived only about 20 days (Fig. 7f). Histological analysis of primary and distant tumor tissues was performed using TUNEL and H&E staining to study the therapeutic effects of CMC-mediated CDT, SDT, and tumor-specific cuproptosis. Figure 7g and S17 show that the CMC + US group had the highest levels of apoptosis or necrosis in primary and distant tumor cells, indicating that CMC-enhanced CDT, SDT, and tumor-specific cuproptosis can induce severe apoptosis or necrosis. ROS staining also showed that CMC-mediated TME modulation and SDT had superior therapeutic effects. Fig. S18 showed that the CMC + US group had the highest levels of ROS in tumor, indicating that the effectiveness of CMC in therapy may be due to the production of a large amount of ROS in tumors.

In vivo immune response evaluation

Apart from the ROS generation in tumor tissues, we then carefully investigated the in vivo therapeutic mechanism of combined CDT, SDT, and tumor-specific cuproptosis through CMC heterojunctions. Evaluating the levels of CRT, HMGB1, and ATP in tumor tissues was the initial step in assessing the ICD effects induced by CMC-mediated SDT/CDT and tumor-specific cuproptosis. The release levels of HMGB1 in each group were measured using ELISA assay. Fig. S19 shows that the CMC + US group had the highest concentration of released HMGB1, indicating that the combined SDT/CDT and cuproptosis effects induced a stronger ICD effect. Additionally, the ATP levels within tumors were highest in the CMC + US group compared to the other groups (Fig. S20). As depicted in Fig. 8a, the immunofluorescence staining images showed a significant increase in the green fluorescence signal of CRT in the CMC + US group as opposed to the other groups.

Next, we investigated the immune responses in both primary and distant tumors in order to understand how the treatment works. In Fig. 8b, it can be observed that the CMC + US group had a greater amount of $CD80^+CD86^+$ mature DCs than the CMC alone group. Specifically, the CMC + US group had the highest number of mature DCs, with a proportion of $CD80^+CD86^+$ DCs at 19.0 ± 3.0% (Fig. 8c). Next, we evaluated the activation of T cells in the spleen and tumors by CMC-mediated synergistic tumor therapy using flow cytometry. Following treatment with CMC and US irradiation, a higher number of $CD4^+CD8^+$ T cells were observed in spleen (Fig. S22), primary tumors (Fig. 8d-f), and distant tumors (Fig. S21). Finally, we assessed the biosafety of Cu_2O and CMC and confirmed the protection effect of Cu-MOF coating. The histopathological testing and hematological analysis were used to evaluate the in vivo long-term toxicity of these treatments. The major organs of the CMC + US group in Fig. S24 showed no significant pathological abnormalities. All markers in the blood biochemistry and blood routine examination for the CMC + US group were within normal levels, suggesting that Cu ions were not released from CMC, as depicted in Fig. S25. We also performed the hemolysis experiments to further investigate the biosafety of CMC. At CMC concentrations as high as 320 μg/mL, red blood cell hemolysis is still not detected (Fig. S26), clearly proving the good biosafety of CMC.

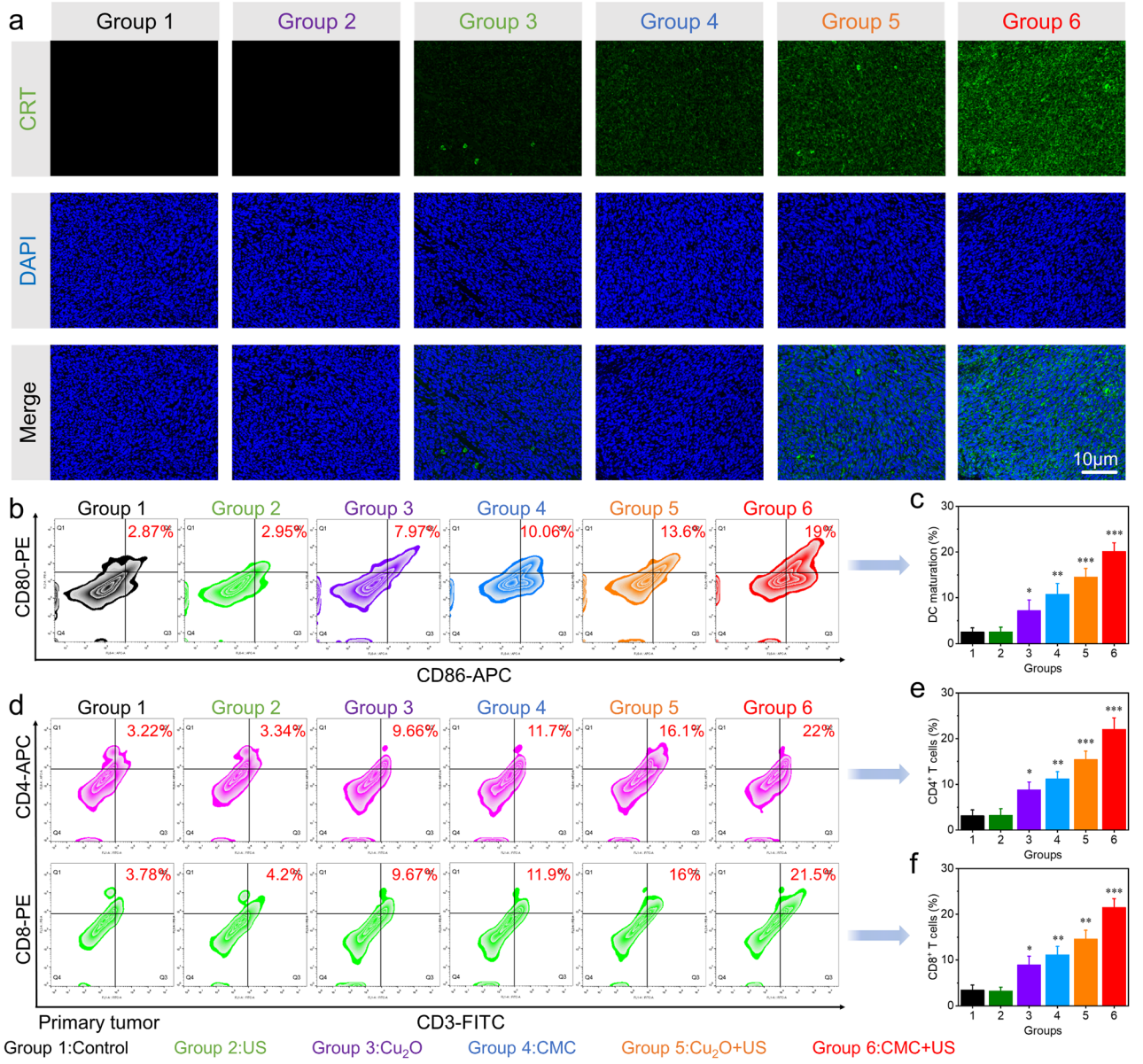

Fig. 8 In vivo immune response evaluation. (**a**) Tumors from different treatment groups were subjected to CRT staining. (**b**, **c**) After undergoing different treatments, the lymph nodes were analyzed using flow cytometry to determine the levels of CD80 and CD86 expression, yielding quantitative results. (**d-f**) Analysis of flow cytometry and quantitative assessment of $CD4^+$ and $CD8^+$ T cell expression in primary tumors of mice post various treatments. ($n = 3$ and $^*p < 0.05$, $^{**}p < 0.01$, $^{***}p < 0.001$)

Conclusion

In conclusion, our approach involves using Cu-MOF as a safeguarding layer to manage the biodegradation processes of Cu_2O. By forming in-situ, the Cu-MOF effectively prevents the non-tumor-specific degradation of Cu_2O nanocubes, ultimately shielding normal tissues from harm. Given the tumor-specific degradation of Cu_2O nanocubes, the potential clinical translation of CMC heterojunctions can be highlighted for its advantages. Despite the inevitable accumulation of CMC in healthy tissues, the mere presence of Cu^+ is insufficient to trigger chemodynamic and cuproptosis effects. This is due to the limited degradation of these heterojunctions occurring mainly in tumors. Second, CDT/cuproptosis can be exclusively activated in tumors because of the tumor-specific release of Cu^+. Moreover, the depletion of GSH by Cu^{2+} causes a domino effect of ROS amplification. Ultimately, by increasing ROS levels and promoting efficient cuproptosis, the immunosuppressive tumor microenvironment can be reversed.

Supplementary Information

The online version contains supplementary material available at https://doi.org/10.1186/s12951-025-03334-w.

Supplementary Material 1

Author contributions
X.C., L.M., and Y.T. performed the main experiments. L.Y. analyzed the data. B.G., Y.Z., and J.Z. designed the project and performed the manuscript writing. All authors have approved the manuscript.

Funding
This work was supported by the National Natural Science Foundation of China (No. 82173649).

Data availability
Data is provided within the manuscript or supplementary information files.

Declarations

Ethics approval and consent to participate
All animal experiments were approved by the Institutional Animal Care and Use Committee of Naval Medical University (IACUC-2012226).

Consent for publication
Not applicable.

Competing interests
The authors declare no competing interests.

Author details
[1]Department of Health Toxicology, College of Naval Medicine, Naval Medical University, Shanghai 200433, China
[2]Jiangsu University, Zhenjiang, Jiangsu Province 212013, China
[3]Shanghai Key Laboratory of Medical Biodefense, Naval Medical University, Shanghai 200433, China
[4]School of Environmental and Chemical Engineering, Shanghai University, Shanghai 200444, China
[5]National Engineering Research Center for Marine Aquaculture, Zhejiang Ocean University, Zhoushan, Zhejiang Province 316004, China

Received: 9 February 2025 / Accepted: 14 March 2025
Published online: 25 March 2025

References

1. Lu X, Zhu Y, Bai R, et al. Long-term pulmonary exposure to multi-walled carbon nanotubes promotes breast cancer metastatic cascades. Nat Nanotechnol. 2019;14:719–27.
2. Peng F, Setyawati MI, Tee JK, et al. Nanoparticles promote in vivo breast cancer cell intravasation and extravasation by inducing endothelial leakiness. Nat Nanotechnol. 2019;14:279–86.
3. Steeg PS. Targeting metastasis. Nat Rev Cancer. 2016;16:201–18.
4. Zhu Y, Yang Z, Pan Z, et al. Metallo-alginate hydrogel can potentiate microwave tumor ablation for synergistic cancer treatment. Sci Adv. 2022;8:eabo5285.
5. Chen Q, Chen M, Liu Z. Local biomaterials-assisted cancer immunotherapy to trigger systemic antitumor responses. Chem Soc Rev. 2019;48:5506–26.
6. De Ruysscher D, Niedermann G, Burnet NG, et al. Radiotherapy toxicity. Nat Rev Dis Primers. 2019;5:13.
7. Luo J, Wang X, Shi Z, et al. Enhancement of antitumor immunotherapy using mitochondria-targeted cancer cell membrane-biomimetic MOF-mediated sonodynamic therapy and checkpoint Blockade immunotherapy. J Nanobiotechnol. 2022;20:228.
8. Sun X, Zhang Y, Li J, et al. Amplifying STING activation by Cyclic dinucleotide–manganese particles for local and systemic cancer metalloimmunotherapy. Nat Nanotechnol. 2021;16:1260–70.
9. Xu J, Lv J, Zhuang Q, et al. A general strategy towards personalized nanovaccines based on fluoropolymers for post-surgical cancer immunotherapy. Nat Nanotechnol. 2020;15:1043–52.
10. Wang M, Chang M, Li C, et al. Tumor-Microenvironment-Activated reactive oxygen species amplifier for enzymatic cascade cancer starvation/chemodynamic /Immunotherapy. Adv Mater. 2022;34:2106010.
11. Wang Y, Gong F, Han Z, et al. Oxygen-Deficient molybdenum oxide nanosensitizers for Ultrasound-Enhanced cancer metalloimmunotherapy. Angew Chem Int Ed. 2023;62:202215467.
12. Guo Y, Wang SZ, Zhang X, et al. In situ generation of micrometer-sized tumor cell-derived vesicles as autologous cancer vaccines for boosting systemic immune responses. Nat Commun. 2022;13:6534.
13. Zhan M, Wang F, Liu Y, et al. Dual-Cascade activatable nanopotentiators reshaping adenosine metabolism for Sono-Chemodynamic-Immunotherapy of deep tumors. Adv Sci. 2023;10:2207200.
14. Li L, Yang Z, Chen X. Recent advances in Stimuli-Responsive platforms for cancer immunotherapy. Acc Chem Res. 2020;53:2044–54.
15. Ngwa W, Irabor OC, Schoenfeld JD, et al. Using immunotherapy to boost the abscopal effect. Nat Rev Cancer. 2018;18:313–22.
16. He C, Duan X, Guo N, et al. Core-shell nanoscale coordination polymers combine chemotherapy and photodynamic therapy to potentiate checkpoint Blockade cancer immunotherapy. Nat Commun. 2016;7:12499.
17. Sun JH, Liang X, Cai M, et al. Protein-Crowned micelles for targeted and synergistic Tumor-Associated macrophage reprogramming to enhance cancer treatment. Nano Lett. 2022;22:4410–20.
18. Chen L, Zhou L, Wang C, et al. Tumor-Targeted drug and CpG delivery system for phototherapy and Docetaxel-Enhanced immunotherapy with polarization toward M1-Type macrophages on triple negative breast cancers. Adv Mater. 2019;31:1904997.
19. Yue Y, Li F, Li Y, et al. Biomimetic nanoparticles carrying a repolarization agent of Tumor-Associated macrophages for remodeling of the inflammatory microenvironment following photothermal therapy. ACS Nano. 2021;15:15166–79.
20. Zhang N, Ping W, Rao K, et al. Biomimetic copper-doped polypyrrole nanoparticles induce glutamine metabolism Inhibition to enhance breast cancer Cuproptosis and immunotherapy. J Control Release. 2024;371:204–15.
21. Deng RH, Zou MZ, Zheng D, et al. Nanoparticles from cuttlefish ink inhibit tumor growth by synergizing immunotherapy and photothermal therapy. ACS Nano. 2019;13:8618–29.
22. Geng B, Hu J, He X, et al. Single atom catalysts remodel tumor microenvironment for augmented sonodynamic immunotherapy. Adv Mater. 2024;36:2313670.
23. He X, Cai J, Hu J, et al. In situ redox of $TiSe_2$ nanoplates to excite Chemodynamic-Enhanced cancer Sono-Immunotherapy. Small Struct. 2024;5:2300558.
24. Liu XZ, Wen ZJ, Li YM, et al. Bioengineered bacterial membrane vesicles with multifunctional nanoparticles as a versatile platform for cancer immunotherapy. ACS Appl Mater Interfaces. 2023;15:3744–59.
25. Zheng RR, Zhao LP, Huang CY, et al. Paraptosis inducer to effectively trigger Immunogenic cell death for metastatic tumor immunotherapy with IDO Inhibition. ACS Nano. 2023;17:9972–86.
26. Wu H, Zhang Z, Cao Y et al. A Self-Amplifying ROS-Responsive nanoplatform for simultaneous Cuproptosis and cancer immunotherapy. Adv Sci 2024:2401047.
27. Lu X, Chen X, Lin C, et al. Elesclomol loaded copper oxide nanoplatform triggers Cuproptosis to enhance antitumor immunotherapy. Adv Sci. 2024;11:2309984.
28. Huang L, Li Y, Du Y, et al. Mild photothermal therapy potentiates anti-PD-L1 treatment for immunologically cold tumors via an all-in-one and all-in-control strategy. Nat Commun. 2019;10:4871.
29. Liu M, Liu B, Liu Q, et al. Nanomaterial-induced ferroptosis for cancer specific therapy. Coordin Chem Rev. 2019;382:160–80.
30. Tsvetkov P, Coy S, Petrova B, et al. Copper induces cell death by targeting lipoylated TCA cycle proteins. Science. 2022;375:1254–61.
31. Chen B, Yan Y, Yang Y, et al. A pyroptosis Nanotuner for cancer therapy. Nat Nanotechnol. 2022;17:788–98.
32. Liu Y, Niu R, Zhao H, et al. Single-Site nanozymes with a highly conjugated coordination structure for antitumor immunotherapy via Cuproptosis and Cascade-Enhanced T lymphocyte activity. J Am Chem Soc. 2024;146:3675–88.
33. Zhou J, Yu Q, Song J, et al. Photothermally triggered copper payload release for Cuproptosis-Promoted cancer synergistic therapy. Angew Chem Int Ed. 2023;62:e202213922.
34. Ning S, Lyu M, Zhu D, et al. Type-I AIE photosensitizer loaded biomimetic system boosting Cuproptosis to inhibit breast cancer metastasis and Rechallenge. ACS Nano. 2023;17:10206–17.

35. Qiao L, Zhu G, Jiang T, et al. Self-Destructive copper carriers induce pyroptosis and Cuproptosis for efficient tumor immunotherapy against dormant and recurrent tumors. Adv Mater. 2024;36:2308241.
36. Zheng J, Ge H, Guo M et al. Photoinduced Cuproptosis with Tumor-Specific for Metastasis-Inhibited Cancer Therapy. Small. 2024;20:2304407.
37. Zhao F, Yu H, Liang L, et al. Redox homeostasis disruptors based on Metal-Phenolic network nanoparticles for chemo/chemodynamic synergistic tumor therapy through activating apoptosis and Cuproptosis. Adv Healthc Mater. 2023;12:2301346.
38. Zhang W, Wang M, Liu B, et al. Glutathione induced in situ synthesis of Cu Single-Atom nanozymes with anaerobic Glycolysis metabolism interference for boosting Cuproptosis. Angew Chem Int Ed. 2024;63:e202402397.
39. Kim BE, Nevitt T, Thiele DJ. Mechanisms for copper acquisition, distribution and regulation. Nat Chem Biol. 2008;4:176–85.
40. Zhu J, You Y, Zhang W, et al. Sensitizing Cuproptosis by endogenous copper-triggered bioorthogonal nanoremodeler. Nano Today. 2024;55:102196.
41. Tian X, Xu H, Zhou F, et al. An intelligent Cupreous nanoplatform with Self-Supplied H_2O_2 and Cu^{2+}/Cu^{+} conversion to boost Cuproptosis and chemodynamic combined therapy. Chem Mater. 2024;36:815–28.
42. Chen W, Xie W, Gao Z, et al. Mild-Photothermal effect induced high efficiency Ferroptosis-Boosted-Cuproptosis based on $Cu_2O@Mn_3Cu_3O_8$ nanozyme. Adv Sci. 2023;10:2303694.
43. He X, Li M, Fan S, et al. Copper peroxide and cisplatin co-loaded silica nanoparticles-based trinity strategy for cooperative Cuproptosis/chemo/chemodynamic cancer therapy. Chem Eng J. 2024;481:148522.
44. Ji M, Liu H, Liang X, et al. Tumor cells are under siege from all sides: tumor Cell-Mimic metal– Organic framework nanoparticles triggering cuproptosis/ferroptosis/apoptosis for Chemo-Chemodynamic-Photothermal-Immunological synergistic antitumor therapy. Chem Eng J. 2024;485:149640.
45. Gao C, Kwong CHT, Wang Q, et al. Conjugation of Macrophage-Mimetic microalgae and liposome for antitumor sonodynamic immunotherapy via hypoxia alleviation and autophagy Inhibition. ACS Nano. 2023;17:4034–49.
46. Hu H, Feng W, Qian X, et al. Emerging nanomedicine-enabled/enhanced nanodynamic therapies beyond traditional photodynamics. Adv Mater. 2021;33:2005062.
47. He Y, Liu HS, Yin J, Yoon J. Sonodynamic and chemodynamic therapy based on organic/organometallic sensitizers. Coordin Chem Rev. 2021;429:213610.
48. Liu M, Ye J, Liu S, et al. Turning silica into enzymes by hydrogenation: simultaneously achieving oxygen vacancy engineering and tumor adaptive accumulation for NIR-II-Potentiated therapy. Adv Funct Mater. 2023;33:2306392.
49. Liu S, Sun Y, Ye J, et al. Targeted delivery of active sites by oxygen Vacancy-Engineered bimetal silicate nanozymes for intratumoral Aggregation-Potentiated catalytic therapy. ACS Nano. 2024;18:1516–30.
50. Zhu D, Zhang T, Li Y, et al. Tumor-derived exosomes co-delivering aggregation-induced emission luminogens and proton pump inhibitors for tumor glutamine starvation therapy and enhanced type-I photodynamic therapy. Biomaterials. 2022;283:121462.
51. Chen H, Luo X, Huang Q, et al. Platelet membrane fusion liposome loaded with type I AIE photosensitizer to induce chemoresistance cancer pyroptosis and Immunogenic cell death for enhancing cancer immunotherapy. Chem Eng J. 2023;476:146276.
52. Shi L, Hu F, Duan Y, et al. Hybrid nanospheres to overcome hypoxia and intrinsic oxidative resistance for enhanced photodynamic therapy. ACS Nano. 2020;14:2183–90.
53. Lucky SS, Soo KC, Zhang Y. Nanoparticles in photodynamic therapy. Chem Rev. 2015;115:1990–2042.
54. Geng B, Hu J, Li Y, et al. Near-infrared phosphorescent carbon Dots for sonodynamic precision tumor therapy. Nat Commun. 2022;13:5735.
55. Dong Z, Feng L, Hao Y, et al. Synthesis of $CaCO_3$-based nanomedicine for enhanced sonodynamic therapy via amplification of tumor oxidative stress. Chem. 2020;6:1391–407.
56. Yi X, Zhou H, Chao Y, et al. Bacteria-triggered tumor-specific thrombosis to enable potent photothermal immunotherapy of cancer. Sci Adv. 2020;6:eaba3546.
57. Xu M, Zhou L, Zheng L, et al. Sonodynamic therapy-derived multimodal synergistic cancer therapy. Cancer Lett. 2021;497:229–42.
58. Son S, Kim JH, Wang X, et al. Multifunctional sonosensitizers in sonodynamic cancer therapy. Chem Soc Rev. 2020;49:3244–61.
59. Zhang Y, Zhang X, Yang H, et al. Advanced biotechnology-assisted precise sonodynamic therapy. Chem Soc Rev. 2021;50:11227–48.
60. Geng B, Xu S, Li P, et al. Platinum crosslinked carbon dot@TiO_{2-x} p-n junctions for relapse-free sonodynamic tumor eradication via high-yield ROS and GSH depletion. Small. 2021;18:2103528.
61. Chan L, Liu Y, Chen M, et al. Cuproptosis-Driven enhancement of thermotherapy by sequentially response $Cu_{2-x}Se$ via copper chemical transition. Adv Funct Mater. 2023;33:2302054.
62. Xu Y, Liu SY, Zeng L, et al. An Enzyme-Engineered nonporous Copper(I) coordination polymer nanoplatform for Cuproptosis-Based synergistic cancer therapy. Adv Mater. 2022;34:2204733.
63. Lu J, Miao Y, Li Y. Cuproptosis: advances in Stimulus-Responsive nanomaterials for cancer therapy. Adv Healthc Mater 2024:2400652.
64. Hu F, Huang J, Bing T, et al. Stimulus-Responsive copper complex nanoparticles induce Cuproptosis for augmented cancer immunotherapy. Adv Sci. 2024;11:2309388.
65. Yu N, Ding M, Wang F, et al. Near-infrared photoactivatable semiconducting polymer nanocomplexes with bispecific metabolism interventions for enhanced cancer immunotherapy. Nano Today. 2022;46:101600.
66. Li J, Yu X, Jiang Y, et al. Second Near-Infrared photothermal semiconducting polymer nanoadjuvant for enhanced cancer immunotherapy. Adv Mater. 2021;33:2003458.
67. Long X, Wang H, Yan J, et al. Tailor-Made autophagy cascade amplification polymeric nanoparticles for enhanced tumor immunotherapy. Small. 2023;19:2207898.
68. Wei Z, Zhang X, Yong T, et al. Boosting anti-PD-1 therapy with metformin-loaded macrophage-derived microparticles. Nat Commun. 2021;12:440.
69. Li Y, Xie J, Um W, et al. Sono/Photodynamic Nanomedicine-Elicited cancer immunotherapy. Adv Funct Mater. 2020;31:2008061.
70. Huang J, Xiao Z, An Y, et al. Nanodrug with dual-sensitivity to tumor microenvironment for immuno-sonodynamic anti-cancer therapy. Biomaterials. 2021;269:120636.
71. Zhu W, Chen Q, Jin Q, et al. Sonodynamic therapy with immune modulatable two-dimensional coordination nanosheets for enhanced anti-tumor immunotherapy. Nano Res. 2021;14:212–21.

Publisher's note